Disponible en ligne sur www.sciencedirect.com
ScienceDirect
C. R. Chimie 13 (2010) 256–269
COMPTES RENDUS CHIMIE

Full paper/Mémoire

Large-pore mesoporous titania-silica thin films ($Ti_{1-x}Si_xO_2$, $0.1 \leq x \leq 0.9$) with highly interdispersed mixed oxide frameworks

Paula C. Angelomé [a], Leandro Andrini [b], M. Cecilia Fuertes [a], Félix G. Requejo [b,c], Galo J.A.A. Soler-Illia [a,c,d,*]

[a] *Gerencia de Química, CNEA, Centro Atómico Constituyentes, Avenue Gral Paz 1499, San Martín, B1650KNA, Argentina*
[b] *Departamento Física, FCE, UNLP and INIFTA-IFLP (CONICET), CC/67 1900, La Plata, Argentina*
[c] *CONICET, Avenue Rivadavia 1917, C1033AAJ, Buenos Aires, Argentina*
[d] *DQIAyQF, FCEN, Universidad de Buenos Aires, Ciudad Universitaria, Pabellón II, C1428EHA, Buenos Aires, Argentina*

Received 20 April 2009; accepted after revision 7 July 2009
Available online 27 August 2009

Abstract

Large-size mesoporous thin films with a mixed titania-silica framework and an $Im\bar{3}m$ cubic-derived or worm-like mesostructure were obtained by combining sol-gel and macromolecular templating techniques. These materials presented accessible mesopores (20 to 25% pore volume), tunable refractive index and high molecular-scale mixing of both ions, as demonstrated by UV-Visible, FTIR and XANES spectroscopy. In addition, a composition effect in the catalytic reduction of silver was found, which permitted one to obtain homogeneous metal nanoparticle-mesoporous film nanocomposites with tuned plasmon position. ***To cite this article: P.C. Angelomé et al., C. R. Chimie 13 (2010).***

Keywords: Sol-gel; Mixed oxides; Mesoporous films; Self-assembly; Catalysis

1. Introduction

The possibility of combining soft chemical materials synthesis methods with supramolecular templates gave birth to the burgeoning area of mesoporous materials. A wide variety of oxide, metal or carbon-based porous matrixes can be obtained, which present organized arrays of monodisperse mesopores (typically 2 to 20 nm diameter) with controlled size, surface and interconnection. These materials represent a great potential in several fields such as catalysis, sensing, responsive materials, biomaterials, environment and energy applications [1]. The formation of these materials is indeed a ''chemical symphony'', in which the co-assembly of ''hard'' inorganic building blocks and ''soft-matter'' elements has to be harnessed in order to reproducibly obtain complex designed materials. Several chemical strategies have been developed towards obtaining a given mesoporous matrix with a well-defined pore system and processing (particles, xerogels, thin films, etc.) [2]. In particular, mesoporous oxide thin films constitute an exciting subject, envisaging advanced coatings (sensors, optoelectronic devices, etc.) [3]. The synthesis of mesoporous thin films by the straightforward evaporation induced self assembly (EISA) [4] pathway has been proven for many different systems,

* Corresponding author.
E-mail address: gsoler@cnea.gov.ar (G.J.A.A. Soler-Illia).

1631-0748/$ – see front matter
doi:10.1016/j.crci.2009.07.001

including Si and transition metal oxides [3]. In the particular case of oxides, an accurate knowledge of the fundamental processes of sol-gel, synthesis and condensation, is necessary in order to set the appropriate conditions that lead to organized, monodisperse pores.

A great number of examples in the literature have dealt with pure oxide mesoporous phases. Mixed oxide mesoporous thin films present an enormous interest due to the possibility of the framework compositional fine tuning, which has an impact on several desired properties such as crystalline structure, refractive index, and surface composition [3]. However, the synthesis of mixed oxide mesoporous frameworks have been less studied, due to the limitations imposed by the different hydrolysis and condensation kinetics of both cations that lead to compositional inhomogeneity throughout the sample [5]. Therefore, it is important to compatibilize the hydrolysis and condensation rates of both centers, in order to tune their reactivity. A series of strategies has been presented so far: mixing the components with different degrees of hydrolysis [6], use of complexing agents to retard the reaction of the most reactive component [7], use of precursors with different reactivities [8,9] or use of mixed molecular precursors [10].

SiO_2-TiO_2 mixed oxide films obtained by sol-gel have been extensively studied for their applications in optics (optical fibers, waveguides or graded refractive index optics), catalysis (tunable acidity coatings) [11], low expansive glasses (ULE®), etc. [5]. Indeed, the incorporation of Ti into a silica matrix or vice versa allows one to:

- obtain materials with tunable refractive index;
- generate sites with different degrees of acidity or surface charge (catalysts);
- retain amorphous phases at high temperatures;
- diminish the reactivity trough dissolution [12];
- functionalize a surface in a selective manner.

Combination of the interesting properties of the Ti-Si mixed oxides with the high specific area and monodisperse pore size typical of mesoporous thin films can lead to an expansion in the range of possible applications. Previous examples of Ti-Si mixed mesoporous oxide synthesis paths have been reported [13–19]. All of them, except two [13,15], report on the preparation of powders in which Ti is the minor component (concentration up to 25% molar). Thus, it is desirable to develop reproducible methods of production of well characterized materials. So far, the characterization presented in previous works is focused on the study of the porosity, mesoscopic order and catalytic activity of the oxides. Some of them also presented spectroscopic characterization [14,16,17,19] (UV-visible, X-ray absorption near edge structure [XANES] or Fourier-transform infrared spectroscopy [FTIR]) or electron microscopy measurements [13,15,17,19]. No studies on the effects of the composition of the oxide were presented previously. Moreover, in most of the previous papers, little reference was made to the homogeneity of the final material.

In this work, a method is presented that allows the reproducible synthesis of mesoporous Ti-Si mixed oxide thin films that are compositionally homogeneous in all the explored composition range (from 0 to 100% of Ti). A detailed structural characterization of these films was performed at two scales: transmission electron microscopy (TEM), 2D-SAXS, X-ray reflectometry (XRR) and ellipsometry were used to probe the mesoscopic order and mesoporosity. Spectroscopic techniques (FTIR, UV and XANES) permit to evaluate the local environment of the cations in the mixed phases, and confirm that intimate mixing is obtained. These detailed studies at the meso- and microscopic level permit one to link the structure and composition effect on the mesoporous film final characteristics.

2. Experimental methods

2.1. Film preparation and processing

Mesoporous Ti – Si mixed oxides thin films were prepared by EISA [4], under controlled deposition conditions, as previously reported for pure oxide films [20]. Non-ionic triblock copolymer Pluronic F127 ($[EO]_{106}[PO]_{70}[EO]_{106}$; EO = ethylene oxide, PO: propylene oxide) that gives rise to pore diameters in the 8 to 10 nm range was used as a template.

The sol composition was $TiCl_4$:$Si(OEt)_4$:F127:-H_2O:EtOH 1-x:x:0.005:10:40 with x varying between 0 and 1. Direct mixing of all the components led to mesoporous films with homogeneous walls albeit locally ordered mesopores. In the Ti-rich range $0 \leq x \leq 0.2$, the solution was prepared by mixing two precursor solutions **A** and **B**, in the appropriate molar ratio. The composition of **A** was $TiCl_4$:F127:-H_2O:EtOH 1:0.005:10:40. The composition of **B** was $Si(OEt)_4$:F127:H_2O:EtOH 1:0.005:10:40, where $Si(OEt)_4$ was previously hydrolyzed in acidic conditions described elsewhere; [21] solution **B** was aged for at least 2 days before mixing with **A**. These conditions ensure homogeneous materials with highly ordered mesopores. A label PH (for pre-hydrolysis) was added to these samples.

All sols were transparent and stable at ambient temperature, and can be re-used several times if conserved in a freezer at −18 °C, and gently restored to room temperature prior to dip-coating.

Precursor solutions were used to produce mesoporous thin films by dip-coating onto silicon wafers or glass substrates under 50% relative humidity at 25 °C, with a withdrawing rate of 2 mm s^{-1}. As-prepared films were submitted to subsequent 24-hour treatments at 50% RH, 60 °C and 130 °C to improve cross-linking of the inorganic network, and favor the formation of ordered micellar arrays. Thermal treatment of these stabilized coatings (up to 350 °C, 2 hours) was performed in a tubular oven, under still air, using 1 °C min^{-1} temperature ramp.

The films were called *TSab* were *ab* represents the molar proportion between Ti and Si in the mixed oxide. For example, a film containing 80% of Ti and 20% of Si was called *TS82*.

In order to compare with the porous films, non porous thin films were prepared in the same conditions described before, but without the template agent.

2.2. Mesostructure and porosity characterization

The film mesostructure was characterized by small angle X-ray scattering (2D SAXS) at the D02A-SAXS2 line at the Laboratório Nacional de Luz Síncrotron LNLS (Campinas, SP, Brazil) [22], using λ = 1.608 Å, a sample-detector distance of ∼690 mm, and a CCD detector (3° incidence).

XRR measurements were performed at the D10A-XRD2 line at LNLS, using λ = 1.5498 Å. Two main parameters are obtained from the XRR data: $\Delta\theta$ between maxima or minima of the reflection and the critical angle (θ_c), defined as the angle in which the intensity is half of the maxima [23].

Thicknesses (t) were obtained from $\Delta\theta$ (with $\theta > 4\theta_c$) using (1):

$$t \approx \frac{\lambda}{2\Delta\theta} \tag{1}$$

Film densities (δ_m) were calculated from the critical angle using (2):

$$\delta_m = \frac{\pi}{N_A \lambda^2 r_0} \theta_c^2 \frac{\sum c_j A_j}{\sum c_j Z_j} \tag{2}$$

where: λ = X Ray wavelength, N_A = Avogadro's number, r_0 = electron classical radius, $c_j = j$ element fraction in the material, Z_j and $A_j = j$ element mass and atomic number, respectively.

Densities of porous (δ_m) and non porous (δ_{mnp}) materials can be obtained with (2). Thus, the materials porosity can be calculated using (3):

$$\text{Porosity}\% = \left(1 - \frac{\delta_m}{\delta_{mnp}}\right) \times 100 \tag{3}$$

Eq. (3) considers a two-phase system composed of the matrix (with δ_m), and void pores.

Ellipsometric porosimetry analysis (EPA) [24] of selected samples permitted to obtain refractive index, thickness and pore size distributions. EPA was performed in a SOPRA GESE5 spectrometric ellipsometer with a controlled vapor pressure chamber. Film thickness and refractive index spectra for single layer thin films were obtained from adjusting the ellipsometric parameters X(λ) and Δ(λ) at each P/P_s value using Win Elli II software. A Cauchy model including Lorentzian peaks in order to model light absorption in the UV spectrum was used to fit the complex refractive index in the 200–800 nm range. Film porosity was evaluated by adjusting a three-medium (air, water, oxide) Bruggeman effective medium approximation (BEMA). Pore size distributions were estimated according to a simple Kelvin model. Pore radii were obtained from the adsorption branches of the EEP; pore necks were obtained from desorption curves [25]. Thickness values obtained by ellipsometry were cross-checked with FE-SEM and XRR measurements; an agreement within 10% was obtained in all cases.

TEM images were collected using a Philips EM 301 transmission microscope (CMA, FCEyN, UBA) operated at 60 kV or a Philips CM 200 Super Twin (UAM, CAC, CNEA) operated at 200 kV and equipped with EDAX®. Samples were obtained by scratching the films from the substrate and depositing them on carbon coated copper grids.

2.3. Framework homogeneity characterization

FTIR were performed on a Nicolet Magna 560 instrument, equipped with a liquid nitrogen cooled MCT-A detector. Films were deposited onto Si wafers (University Wafer, South Boston, MA), transparent in the IR region.

UV-visible measurements were performed on a Hewlett Packard 8453 spectrophotometer equipped with a diode array detector, in the 200–1000 nm range. For these measurements, films were deposited on Pyrex 7740 glass (University Wafer, South Boston, MA), transparent in the UV-visible region.

Ti K-XANES spectra were acquired using a fluorescence detector and a Si(1 1 1) monochromator

at the D04B-XAS beamline of the LNLS [26]; the resolution was about 0.8 eV. The beam intensity was measured using an ionization chamber filled with air at room temperature. Photon energies were calibrated during the experiments in transmission mode by using a Ti foil placed between the two ion chambers located at both sides of the reference sample and setting the first inflection point at the known absorption edge energy of Ti^0 (4966 eV).

The region of the absorption spectra below 4960 eV was fitted with a Victoreen function to subtract the background contributions throughout the entire energy range. Absorption intensities were normalized by their average value between 5050 and 5200 eV [27]. Four features in the pre-edge region were identified, in agreement with previous studies [28–30]. After background subtraction and normalization, this region was fitted with four Gaussian peaks [31], labelled in ascending energy as A1, A2, A3, and B [29,32] (Supplementary information, SI).

Si K-XANES spectra were acquired in total electron yield mode (TEY) and using a InSb(1 1 1) monochromator at the D04A-SXS beamline of the LNLS [33]. The beam focalization was performed using a Rh mirror. The incident photon energy was in the range of the Si K-edge for the experiments. The resolution was about 1 eV. The I_0 beam intensity was measured using a thin foil of Al located before the main chamber. The photon energies were calibrated in TEY mode using a Si foil and setting the first inflection point to the energy of the K absorption edge of Si^0 (1839 eV). Two polynomials functions were fitted to discount the background and normalize the spectrum, one for the pre-edge region and the other for the region beyond the edge. After background subtraction and normalization, the white line (WL) region was fitted using Gaussian peaks (SI).

2.4. Ag nanoparticle synthesis

Ag NPs were synthesized within the mesopore systems of the thin films as follows: calcined mesoporous films were immersed in a 1:1 water:ethanol mixture of $AgNO_3$ 0.05 mol dm^{-3} for 15 minutes. Then, 7% w/w formaldehyde (HCHO) solution was added until a 1% w/w final concentration was reached and left under stirring for 3 hours. After 15 to 20 minutes, a noticeable change in color was observed in the mesoporous films; coloration was more intense in films containing higher titania loadings. Silver loading (i.e., the pore volume fraction occupied by the nanoparticles) was obtained from the analysis of the critical angle in XRR measurements, as previously described [34]. In order to obtain accurate density values, measurements were done under dry nitrogen flux, to avoid atmospheric water condensation within the pores that leads to the underestimation of mesoporosity.

3. Results and discussion

3.1. Synthesis and structural characterization

Mesoporous thin films were obtained by dip-coating under controlled conditions followed by careful post-processing. Two important factors were kept in mind, taking into account the sol-gel chemistry of the precursor solutions. The hydrolysis and condensation behaviour of both ions have to be matched in order to control order at two length scales: (a) molecular, i.e., walls with homogeneous composition, (b) mesoscopic, i.e. ordered arrays of monodisperse pores. Film samples were prepared either by a direct mixture of $TiCl_4$ and TEOS (all the Ti:Si ratio were explored) or by combining $TiCl_4$ and a prehydrolized solution of $Si(OEt)_4$, in the Ti-rich samples ($0 \leq x \leq 0.2$, x being the Si fraction in the mixed oxide).

Mesoporous oxide thin films with different degrees of order are obtained under the studied conditions, as can be seen in the TEM pictures and 2D-SAXS patterns showed in Fig. 1. Results are summarized and compared with the results obtained for the pure oxides in Table 1. All samples produced under the reported synthesis conditions appear homogeneous under TEM observation. No sharp contrast variation corresponding to massive phase separation (''islands'') [9] was observed in the micrographs, and metal ratios estimated by EDS presented homogeneous values along the samples (Fig. 1c). This is a first hint of framework homogeneity, at least at the mesoscopic level. These observations were confirmed by spectroscopic techniques, as detailed below.

Mesostructure, interpore distances and mesostructure contraction for samples heated at 200 °C were obtained from 2D-SAXS patterns. Samples derived from a direct mixture of the precursors lead to mesoporous oxides with local pore order throughout all the mixture range. Interpore distances in these samples shown in Table 1 were calculated from 3° or 90° patterns. For silica-rich systems ($0.5 \leq x \leq 0.9$), some influence of the Ti(IV) is observed, and pore size becomes smaller than in pure mesoporous silica with increasing Ti content; the obtained interpore distance values tend to 12.5 nm, similar to those observed in PH systems or pure titania. For $x \leq 0.5$, interpore distances are significantly higher (ca. 14 nm), and correspond

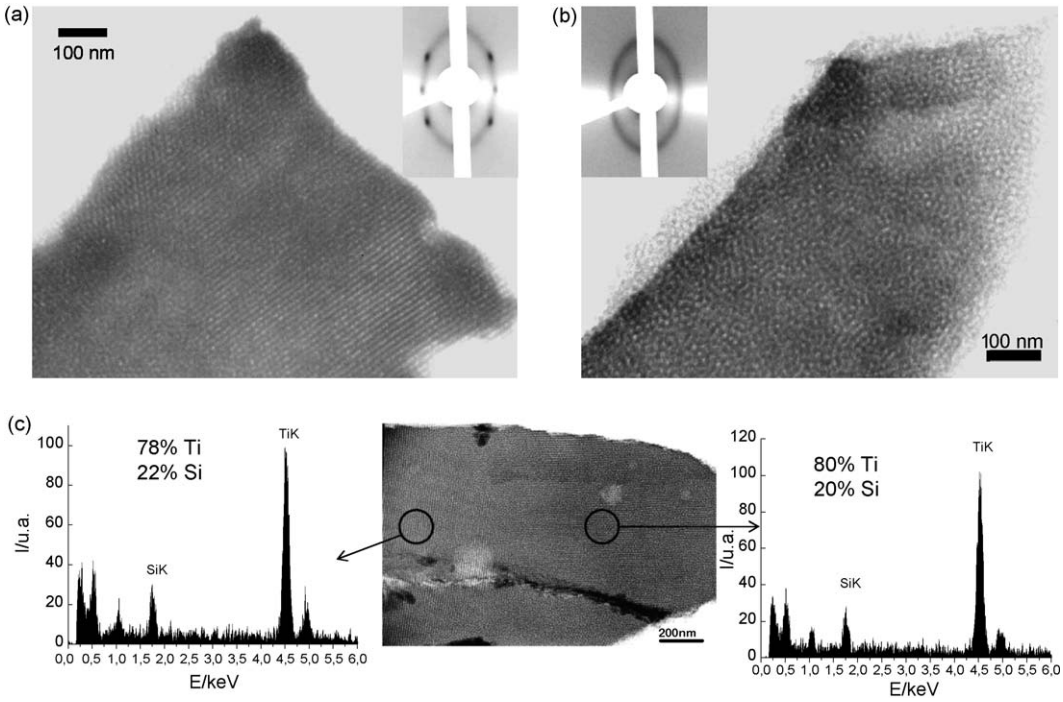

Fig. 1. TEM and SAXS characterization (inset) of titania-silica mesoporous mixed oxides: a: *TS91PH* cubic mesostructure; b: *TS19* local organized pore structure; c: TEM of a *TS82PH* cubic sample, showing two EDS spectra obtained at different sample locations.

roughly to worm-like systems such as those observed in F127 templated worm-like titania obtained in conditions where condensation is favored (high temperature) [35]. In the case of titania-rich prehydrolyzed samples (PH, $x \leq 0.5$), the analysis of 2D-SAXS patterns reveals that the interplanar (110) distances for cubic $Im\bar{3}m$ samples are in the 12.5 to 12.7 nm range, thus the cubic pattern a = 17.5 to 18 nm, in agreement with previously reported mesoporous titania [20]. In all cases, whether in the case of prehydrolyzed or direct mixing samples, mesostructure contraction for samples heated at 350 °C does not strongly depend on the composition of the oxide (all in the 40 to 50% range, Table 1). It has to be mentioned that samples heated at 350 °C are amorphous, and no wall crystallization process is evident until at least 700 °C in the examined samples; a similar behaviour has been reported in other mixed mesoporous oxide systems containing Si(IV) [9].

Table 1
Mesostructures and mesostructural parameters of mixed oxide mesoporous film samples.

Sample[a]	x	Mesostructure	d_{110}/nm	d_{110}/nm	Contraction/%
SiO_2	1	$Im\bar{3}m$ cubic	14.6	7.6	48
TS19	0.9	Local order	13.2	7.6	42
TS28	0.8	Local order	12.5	6	52
TS55	0.5	Local order	13.7	7.2	47
TS82	0.2	Local order	14.3	8.4	41
TS91	0.1	Local order	14.1	8.3	41
TS82PH	0.2	$Im\bar{3}m$ cubic	12.5	7.6	39
TS91PH	0.1	$Im\bar{3}m$ cubic	12.4	7.6	39
TiO_2	0	$Im\bar{3}m$ cubic	12.7	6.6	48

[a] *TSab* describes the sample composition, see Experimental; the PH label indicates that a silica prehydrolyzed solution was used as precursor.

These results are the consequence of complex behaviour of the reacting systems at several length scales. Pore ordering and compositional homogeneity of metal centers depend strongly on the compatibility of the hydrolysis–condensation processes of the inorganic precursors [36]. In particular, it has been observed that conditions where condensation is favored lead to poorly ordered mesophases, due to the increased viscosity in the freshly formed liquid film that hampers reorganization from an initially locally ordered mesophase [37]. In the case of direct mixture systems, an increase in the condensation degree of the silica precursors with increasing Ti quantities could be due to the well established fact that small amounts of transition metal catalyze Si(IV) hydrolysis and condensation [38–40]. The higher the titanium contents, the larger the silica condensation rate should be, leading to more disordered pore arrays. On the other

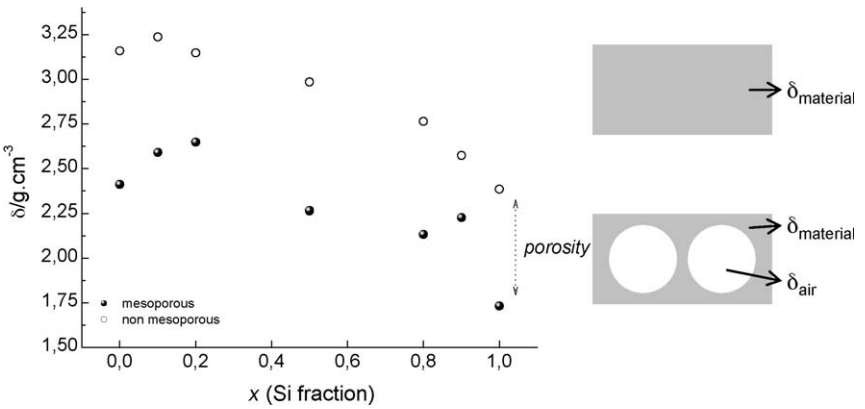

Fig. 2. Dependence of film density with the Si fraction (x) of non-mesoporous (○) and mesoporous (●) mixed oxide thin films, produced by dip-coating at a withdrawal speed of 2 mm s^{-1}, and calcined up to 350 °C. The scheme (right) shows the models used for the calculation of film density.

hand, the use of pre-hydrolyzed silica can lead to smaller Si-oxo clusters with diminished reactivity in the presence of Ti(IV) centers, permitting a certain flexibility of the inorganic networks. This could explain the more extended organization observed in PH systems.

In the following, only Si-rich films formed by a direct mixture of the precursors ($0.5 \leq x \leq 0.9$) and Ti-rich films formed under PH conditions ($x \leq 0.5$) will be discussed; these were the most reproducible conditions to obtain homogeneous mesoporous samples.

XRR permits one to accurately evaluate film density and thickness [23]. Figure 2 shows the dependence of the mass density of non-mesoporous and mesoporous films, obtained from the critical reflection angle, with the silicon content, x. Film composition was considered close to the nominal composition values, as confirmed by EDS measurements. Film thicknesses, densities and porosities calculated from XRR measurements are displayed in Table 2. According to XRR measurements, the thicknesses are slightly higher for the films containing higher concentrations of Ti, due to the increase in sol viscosity [5]. Film density remains relatively constant up to $x \leq 0.2$ and decreases more markedly as x increases for $x \geq 0.5$. These trends coincide well with the densities of the non-mesoporous mixed oxides, as shown in Fig. 2. Substitution of Ti by Si leads to a change in the inorganic matrix density. In this situation, there is little density variation when the less dense oxide is incorporated in the denser one and more notorious variations in the opposite case.

Table 2
Thickness and porosity data obtained from XRR for films of Table 1.

Sample	x	Film thickness/nm	Density/g cm^{-3}	Porosity/%
SiO_2	1	158 ± 7	1.733	27
TS19	0.9	115 ± 6	2.228	13
TS28	0.8	113 ± 5	2.134	23
TS55	0.5	140 ± 12	2.265	24
TS82PH	0.2	169 ± 16 (178 ± 3)	2.648	16 (20)
TS91PH	0.1	193 ± 15	2.59	20
TiO_2	0	184 ± 12	2.411	24

Data in parentheses are obtained from EPA, for selected data.

The density changes are closely related to refractive index variations, a material feature that is crucial for many of the projected applications of the mixed oxide thin films. Furthermore, in all the compositional range the porosity of the films, reflected in the difference between both curves in Fig. 2, remains almost constant. Therefore, it is possible to vary the refractive index of the thin film by changing the composition without losing porosity.

The XRR-derived porosity results were checked by EPA. Fig. 3 shows the EPA analysis of a *TS82PH* sample, and the resulting narrow pore size distribution, coherent with a highly ordered pore array. Pore diameters and interpore openings can be estimated at 7 and 3.7 nm, from the analysis of the adsorption desorption curves, respectively. In the case of a Si-rich worm-like sample such as *TS19*, pore distributions are somewhat less well-defined, probably due to a higher pore size dispersion. Both analysis techniques yield comparable results; indeed, XRR estimations constitute an excellent seed to initial EPA calculations. Overall, these two techniques demonstrated that mixed mesoporous oxides with a narrow distribution of accessible pores and a gradient of density (therefore, of refractive index) can be produced.

3.2. Spectroscopic characterization

FTIR, UV visible and XANES spectroscopic techniques were used to evaluate the interdispersion

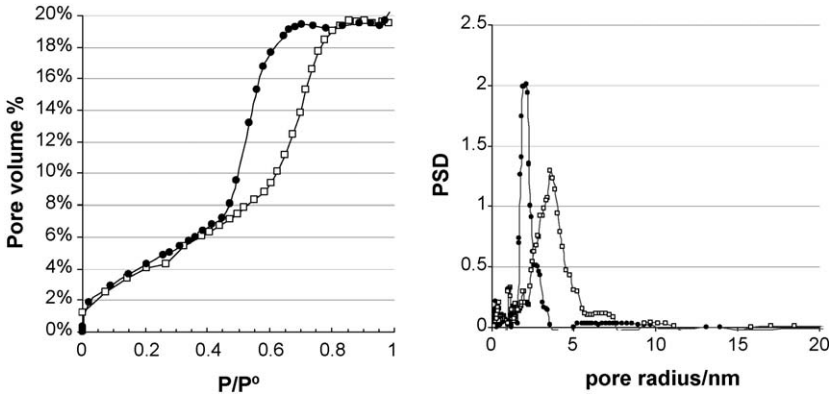

Fig. 3. Left: water adsorption (□) and desorption (●) curves obtained by Ellipsometry Porosity Analysis (EPA) of a *TS82PH* mesoporous film produced by dip-coating (silicon substrate, withdrawal speed 1 mm s^{-1}, thermal treatment 350 °C). Right: pore size distribution obtained from both curves following a simple Kelvin model (WinElli II software, SOPRA, Inc.).

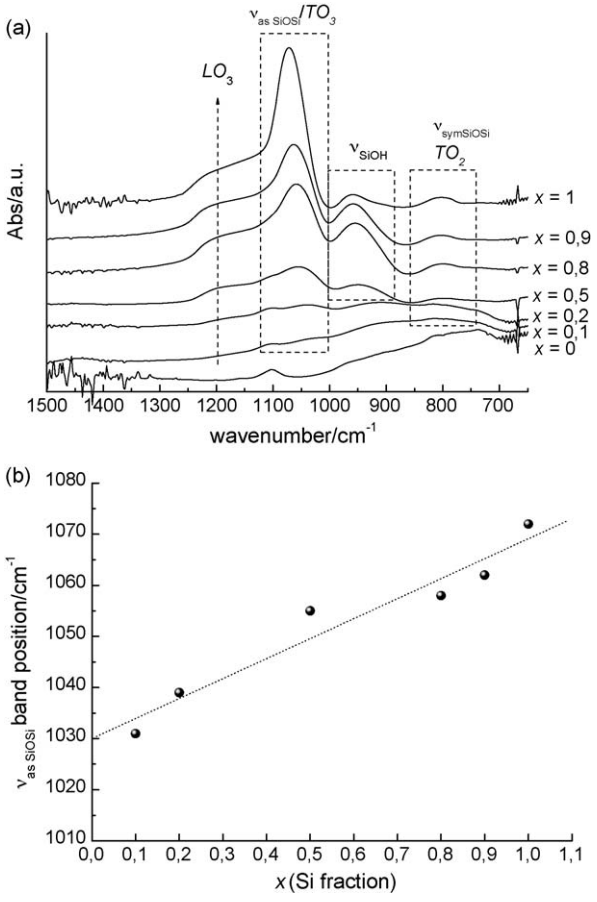

Fig. 4. a: FTIR absorption spectra in the 1500–600 cm^{-1} region for mixed oxide thin films calcined to 350 °C. Compositions and significant bands are indicated in the figure; b: evolution of the asymmetric Si-O-Si TO_3 band position with the Si contents, *x*, for samples shown in (a).

of the mixed oxide and the local environment of the different ions that compose the oxide framework.

FTIR analysis allows a straightforward determination of important information about mesoporous oxides, in particular, the presence of the template, and the existence of bands attributed to mixed oxides. All the spectra were acquired before and after thermal treatment and thoroughly analyzed in the 1500–650 cm^{-1} region. Fig. 4a displays the FTIR spectra of all the oxides synthesized in this work, treated at 350 °C, with band assignation according to literature [41]. Three bands associated to the Si—O—Si bond are observed: LO_3 at ~1200 cm^{-1}, $\nu_{as\ SiOSi}$ (TO_3) at ~1050 cm^{-1} and $\nu_{sym\ SiOSi}$ (TO_2) at ~800 cm^{-1}. A medium intensity band that can be associated to superposition of ν_{SiOH} and titania-silica vibrations is also observed at 950 cm^{-1} (see discussion below). The results for the films treated at 130 °C (Figure S4 in supplementary information) are analogous but harder to interpret due to the presence of intense bands of the template molecule (ν_{COC} around 1100 cm^{-1}, **SI**) that hinder a proper observation of the framework bands.

As the Si proportion decreases, two main trends are observed in the spectra: a decrease in the intensity of the $\nu_{sym\ SiOSi}$ and a displacement of the $\nu_{as\ SiOSi}$ to lower wavenumbers.

The first trend has been attributed to the disruption of the order in the SiO_2 framework [9,42] as the Ti concentration increases. This signal is indicative of an extended interface between Si and Ti, which implies a good interdispersion in the mixed oxide.

The second observation, the displacement of the $\nu_{as\ SiOSi}$ to lower wavenumbers as Ti concentration

increases, is coincident with previous observation in Zr-Si mixed oxides [43–45]. It has been proposed that the position of the Si—O—Si asymmetric vibration is an indicator of the oxide dispersion. The displacement is attributed to an increase in the oscillator reduced mass (that changes from Si—O—Si to Ti—O—Si) and the corresponding bond vibration frequency reduction. In fact, this is reflected in the continuous relationship between the band position and the oxide composition displayed in Fig. 4b.

Regarding the bands located around 950 cm^{-1}, the analysis is less straightforward. These bands are clearly observed in samples treated at 130 (**SI**) and 350 °C (Fig. 4a). Qualitative comparison of these bands with the silica framework TO_3 signal (ca. 1050 cm^{-1}) for each sample suggests that the 950 cm^{-1} signals are intense for high silica content samples. It is not possible to extract more accurate quantitative information, due to the fact that spectra have been obtained at ambient conditions, around 40 % relative humidity, and they have not been normalized. According to the literature, absorption in this region can be mainly attributed to two processes:

(a) sol-gel derived silica films presenting high surface area, or before full densification, exhibit a band of medium intensity centered near 940–960 cm^{-1} due to Si–OH stretching vibrations, overlapped, or coincident with $Si–O^-$ groups [41];
(b) previous work on mixed Ti-Si oxides attributes the band to Si-O-Ti vibrations [46]. This assignment has been confirmed with isotopic exchange between ^{16}O and ^{18}O in dehydrated samples of a Ti-zeolite composite [47].

Under our explored conditions, the most likely hypothesis is that the infrared absorption observed in the 950 cm^{-1} region could be ascribed to the superposition of both kinds of bands. This can explain the noticeable band at $x = 0$, as well as the qualitative absorption increase for mixed oxide bands with increasing Ti concentration for low titania contents ($x < 0.5$), where ν_{SiOH} due to surface groups can be important.

UV – visible absorption has been proven to be a useful tool to determine the coordination of transition metals such as Ti in solids or complexes. UV-visible spectra of mixed and pure oxides prepared in this work are presented in Fig. 5. Depending on Ti concentration, the observed bands can be attributed to Ligand to Metal Charge Transfer (LMCT) from O^{2-} to Ti^{4+} isolated

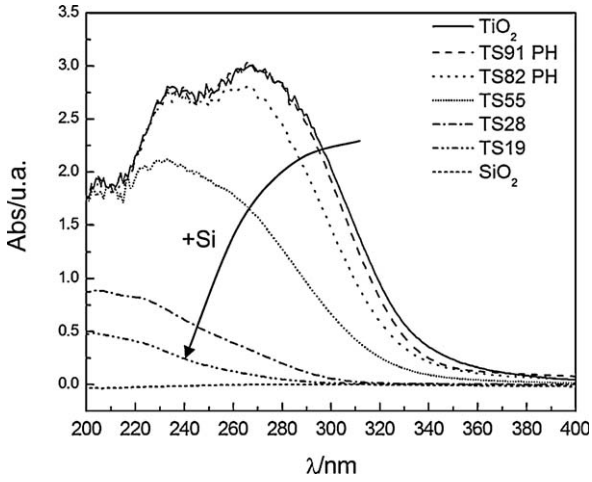

Fig. 5. UV-visible spectra of mixed oxide thin films calcined at 350 °C.

centers, or to electron transfer between valence and conduction bands in the mixed oxide.

A continuous behaviour is clearly observed: those oxides having a high concentration of Ti, with spectra closely related to pure TiO_2, and those oxides having high concentration of Si, with spectra closely related to pure SiO_2, *TS55* being an intermediate case. Spectra of *TS91* and *TS82* present the same three absorption peaks attributable to the TiO_2 band structure (206, 235 and 267 nm), with a slight shift in the position of the absorption border (263 nm in *TS82*) to lower λ. Less intense absorption bands in *TS55* are observed at 206, 231 and 258 nm. On the other hand, in the case of *TS28* and *TS19* two or one band of lower intensity can be distinguished at 205 and 220 nm, clearly displaced to lower λ values respect to pure TiO_2. This band shift to lower wavelengths as Ti concentration decreases (or x increases) has been previously observed by UV diffuse reflectance in several Ti-Si mixed oxides prepared by sol gel method [48–51]. Moreover, the band position has been related to different local environment of the Ti center surrounded by O atoms, as shown in Table 3. A clear tendency is deduced from the literature data: isolated tetrahedrically coordinated Ti centers appear at lower λ; as the coordination number increases from 4 to 6 (octahedral coordination), the band is displaced to higher wavelengths.

According to this correlation between coordination number and position of the absorption band, it can be proposed that when Ti is the minor component of the mixed oxide, its coordination is lower and closer to the one of Si in SiO_2 (4). In contrast, when Ti is the major component, its coordination number is close to the one

Table 3
UV-visible band assignment for titania centres.

Environment	λ_{max}/nm	References
Anatase	380	[50,66]
Rutile	410	[50]
Isolated T_d	200–220	[16,18,48,51,67]
Isolated O_h	230–275	[14,16,18,51,67]

of Ti in the TiO_2 matrix (6). The Ti capability to act as a network modifier of silica, having a coordination around 4, has been previously demonstrated [5,7b]. These observations about the coordination number of the Ti are another proof of the high degree of mixing that present the mixed oxides prepared in this work. The band shift to higher energies (lower λ) with increasing Si contents can be attributed to two different phenomena:

- formation of TiO_2 clusters of lower size as Si concentration increases. The lower size of the aggregates is correlated with an increase in the transition energy, due to *quantum size effect* of semiconductors [50,51];
- a continuous modification of the band structure of the oxide and a separation of the bands as going through SiO_2 (higher E_{gap}) to TiO_2 (lower E_{gap}).

The first hypothesis implies that the mixed oxides are not really mixed at the atomic scale, (but are still mixed at TEM-EDS level). The second one implies the formation of mixed oxide at the atomic level.

In order to confirm the high interdispersion of the inorganic centres in the matrices, XANES experiments at the Ti and Si K-edges were performed. Fig. 6 shows the Ti K-XANES spectra for the extreme samples: a. *TS19*, b. *TS28*, c. *TS82*, and d. *TS91*, and amorphous TiO_2 (am-TiO_2) and anatase TiO_2 (a-TiO_2) reference compounds.

The relationship between position and intensity of pre-peaks provides information on the coordination number of the absorbent atom [52]. In particular, it has been observed that the peak intensity decreases while the corresponding energy increases with the center-symmetry degree of the absorbent. In the Ti K edge pre-peaks region, a very intense peak is observed, which is associated with tetrahedrical symmetry, shifted 3 eV towards lower energy than in the case of less intense pre-peaks associated with octahedral symmetry [52].

The pre-edge features in Ti K-edge XANES spectra of a-TiO_2 consist in four peaks (labeled as A1, A2, A3 and B [53], SI). A1 corresponds to $1s \rightarrow 3d$ quadrupolar transitions [53,54], while A2 plus A3 and B peaks correspond to transitions from the Ti 1*s* to t_{2g} and e_g bands respectively [29]. Even if the definitive description of the origin of the pre-peaks is still open, it is known that A2 has higher intensity for XANES spectra of Ti compounds with low coordination [53–55], directly reflecting the very small size of nano-domains of TiO_2 through the increment of the A2 intensity [56]. The dipolar transitions 1*s*-*np* are contained in a region between 4980 and 5020 eV [52].

The spectra in Fig. 6 can be quantitatively described by adjusting the positions and areas of four peaks at the pre-edge region, which was fitted with Gaussian curves A1, A2, A3, and B, and a Gaussian shape for background. Taking into account the spectra of am-TiO_2 and a-TiO_2, it can be stated that even the sample

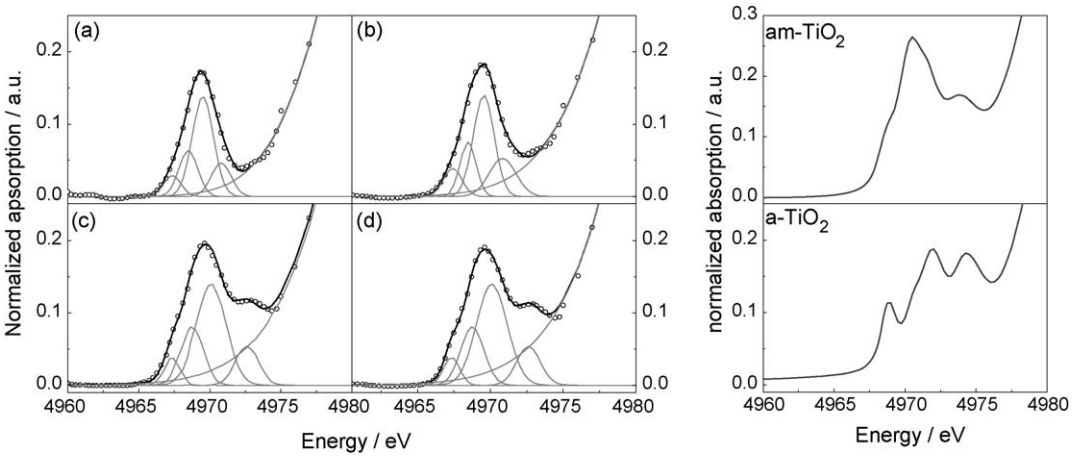

Fig. 6. Ti K-XANES pre-peak region spectra for the studied samples: a) *TS19*, b) *TS28*, c) *TS82*, and d) *TS91*, and (on the right) amorphous TiO_2 (am-TiO_2) and anatase TiO_2 (a-TiO_2) reference compounds.

with higher Ti contents (*TS91*) presents amorphous characteristics.

In previous papers [31,57] we proposed a methodology to determine the relative fraction of Ti with varying coordination number. The local symmetry of Ti with six near neighbours (oxygen atoms) can be associated with Ti in crystalline TiO_2 anatase [32]. The same type of analysis developed here on the average coordination number *N*, indicates the presence of a fraction of crystalline (local Ti environment) TiO_2 less than 45% in the *TS91* film. Therefore, even the presence of small silica quantities disrupts the Ti-O-Ti network.

A numerical fitting of the peaks in the pre-peak region with Gaussian curves shows a broadening and shifting position towards higher energies for A3 in the samples *TS82PH* and *TS91PH* (Fig. 6). As reported by Farges et al. [52], this corresponds to an increase in the coordination number (from $n = 4$ to 5). The increase in the coordination number should correspond to the coexistence of am-TiO_2 (with a fraction of Ti sites with $n = 4$) with crystalline a-TiO_2 (where Ti sites have $n = 6$). Mountjoy et al. [58] have shown that the presence of small amounts of Ti in SiO_2 induce the decrease of the Ti coordination number because of the lower coordination of Si. This fact is evidenced by present XANES results obtained at the pre-peak region.

As it was mentioned, peaks at A2 plus A3 and B regions correspond to transitions from the Ti 1*s* orbital to t_{2g} and e_g bands, respectively. Fig. 6 shows a change of position and intensity of peak B, in addition to changes in intensity of A2 and A3 peaks. These correspond to variations at t_{2g} and e_g bands due to the change in the structural configuration of Ti environment. The position of B in the *TS28* and *TS19* samples is similar to the corresponding position in Ti K-XANES spectra of a-TiO_2. In samples with low percentage of Ti the transitions to the e_g band are partially forbidden. This is in close agreement with UV-visible results, which indicates the presence of two different types of samples: those samples having a high concentration of Ti, with spectra closely related to pure TiO_2, and those having high concentration of SiO_2, with spectra closely related to Ti included in SiO_2.

On the other hand, Natoli's rule [59] allows a simple correlation between the energy difference ΔE of the resonance peaks [60] (Fig. 7) with the distance *r* between scatter neighbours and their ligands, expression (4). The corresponding values obtained for Ti – O distances in our samples using this rule are shown in Table 4.

$$\Delta E.r^2 = \text{const} \quad (4)$$

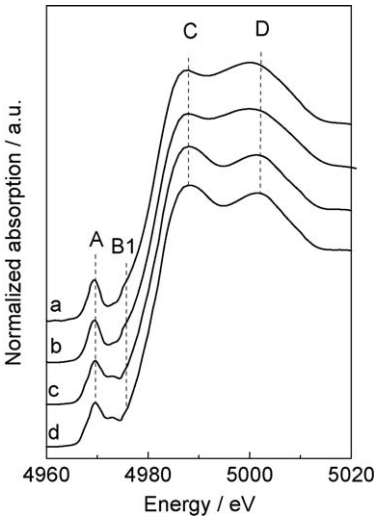

Fig. 7. Ti K-XANES spectra for the studied samples: a: *TS19*; b: *TS28*; c: *TS82PH* and d: *TS91PH*. The resonant peaks C and D (dotted vertical lines) were utilized for obtaining the simple correlation between the energy difference ΔE of the resonance peaks with the distance *r* between scatter neighbours and their ligands (Eq. (4)).

Table 4
Position of the peaks C and D (Fig.7).

Samples/FTO (molar %)	C (eV)	D (eV)	Ratio (Natoli's rule)
TS19	4987.7	4999.5	$3.4r_{TS19} = a$[a]
TS28	4987.8	4999.5	$3.4r_{TS28} = a$
TS82	4987.7	5001.2	$3.7r_{TS82} = a$
TS91	4987.9	5001.5	$3.7r_{TS91} = a$
References			
am-TiO_2	4988.7	4999.9	$3.3r_{amof} = a$
a-TiO_2	4985.4	5002.5[b]	$4.1r_{anat} = a$

This energy position was obtained from the zero of the first derivative of XANES spectrum. From these peak positions the distance *r* between neighboring scatterers and absorbent atom (i.e. Ti-O bond) were determined applying Natoli's rule (Eq. (4)).

[a] *a* is the same constant for all determinations (Eq. (4)).

[b] Position of the peak with highest energy of the three resonances in the corresponding region for anatase.

Taking into account the comparison of the Ti-O distances between am-TiO_2 and a-TiO_2 (Table 4), it can be noted that the Ti-O first neighbour distance in the a-TiO_2 compound is shorter than in am-TiO_2. This is consistent with a simple electrostatic consideration, which indicates that a more orderly electrostatic ion configuration is adopted for the minimum energy. This energy is precisely reached by minimizing the Ti-O distance in the a-TiO_2 compound. On this basis, it can be assumed that the shorter Ti-O distance indicates a greater degree of local crystalline order. This is in agreement with the results reported by Mountjoy et al.

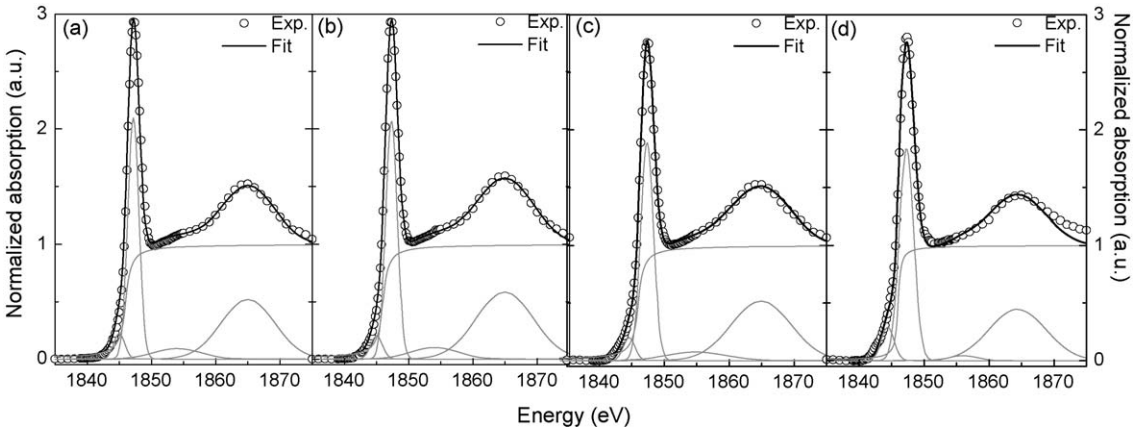

Fig. 8. Si K-XANES spectra (hollow circles) and fitted curves (solid lines) for the studied samples: a: *TS19*; b: *TS28*; c: *TS82PH* and d: *TS91PH*.

[61] (and reference therein), where it is also reported that the coordination number of Ti increases with the increase of the molar concentration of TiO_2 in TiO_2-SiO_2 mixed oxide xerogels.

On the other hand, an inspection of Si K XANES spectra (Fig. 8) shows that all spectra have a similar feature than those corresponding to Si in SiO_2. This region of the spectrum corresponds to the dipolar transition $1s \rightarrow t_2$ (Si 3*p*-3*s*) [62].

A complete replica of the XANES spectra can be obtained by fitting with four Gaussian curves [63]. The first one (A) centered at 1844.34 eV is attributed to the forbidden electronic transition $1s \rightarrow a_1$ (Si 3*s*-3*p*) (because for this transition $\Delta l = 0$). The second one corresponds to the white line (B), centered at 1847.05 eV, associated with the $1s \rightarrow t_2$ (Si 3*p*-3*s*) transition. A third one (C) at 1853.50 eV is due to the $1s \rightarrow e$ (Si 3*d*-3*p*) transition and finally the fourth one (D) at 1863.66 eV corresponds to the $1s \rightarrow t_2$ (Si 3*d*-3*p*) transition.

The more noticeable difference between the spectrum of the reference compound and the samples is the lower intensity of the white line (WL) for the latter. The mentioned area is about the same for all samples and also with respect to the amorphous SiO_2. The only confident difference between areas, but minor, can be found in peak A. In effect this higher intensity for this forbidden transition in the spectra corresponding to samples with lower Si content suggests the lower symmetry for Si sites when this element is highly diluted in the sample. This is the only fact affected because the fraction of Ti present in the sample, being the remains aspects constant.

In conclusion, a set of spectroscopic techniques permits one to confirm the high interdispersion of Ti and Si centres attained by this synthesis path. Bonding of Si centres to Ti along all the composition axis has been evidenced by shifts in the Si-O-Si vibration modes. UV-Vis and XANES spectroscopy permitted to corroborate two limiting behaviors for Ti(IV) centres: at low concentration ($x \geq 0.8$), Ti substitutes Si in tetrahedral sites, the coordination increases steadily for larger Ti:Si ratios. The conditions of sample preparation chosen here seem to preclude extended condensation of silica and titania species, thus leaving the opportunity to create flexible mixed building blocks that lead to non-segregated mixed mesoporous oxides.

3.3. Selective catalytic properties of mixed mesoporous thin films

One of the interests in high-area mixed oxides is the possibility to combine two metal centres with different acidity, in order to be able to regulate processes such as heterogeneous catalysis. The mesoporous mixed oxide films developed and characterized in the preceding sections present interesting properties regarding tuned reactivity towards metal reduction. It is well known that chemical reduction of silver is favored on the surface of transition metal oxides. Recently, this concept was applied in order to selectively deposit silver nanoparticles within mesoporous titania films [34]. The presence of a titania framework seemed decisive to trigger a fast formation of silver nanoparticles in the pore system, presumably by enhancing the reactivity of the reducing agent, formaldehyde. In order to test an eventual role of Ti(IV) centres in the reduction process, mesoporous mixed oxide films with variable composition were put in contact with solutions containing formaldehyde (1% w/w) and Ag^+ (0.05 mol dm^{-3}) for a fixed period of 3 hours. XRR measurements permitted one to determine the pore volume fraction loaded with

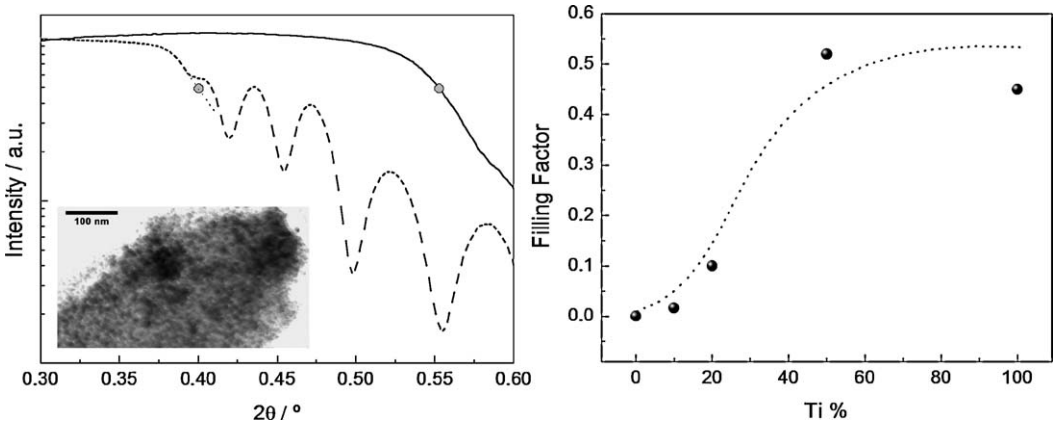

Fig. 9. Left: XRR spectra of *TS55* before (dashed line) and after (full line) impregnation with Ag^+-formaldehyde solution. Critical angles are indicated by grey circles. Inset shows a TEM image of a silver-loaded *TS55* film. Right: Change of the pore fraction filled with silver nanoparticles with the Ti contents of the matrix, after 3 hours silver reduction. The dotted curve is a guideline for the eye.

metal. A typical XRR diagram of empty and loaded films, and the pore volume occupied by Ag nanoparticles in films with varying composition are displayed in Fig. 9. It can be observed that nanoparticle growth within the pore systems due to Ag^+ reduction is notoriously favored in samples containing a higher Ti fraction, for a fixed reduction time. This fact demonstrates that mesoporous films with a tuned framework composition present a controlled catalytic behaviour for the production of nanoparticles. In addition, these films presenting a continuous variation of refractive index lead to the modification of the silver plasmon position and intensity (Supplementary information), due to matrix-nanoparticle interactions [64]. This is an example of the use of two different features of the same film (refractive index and catalysis) in order to obtain nanocomposites with tailored properties.

4. Conclusions

A method of producing mesoporous mixed oxides with a highly interdispersed Ti-Si framework along all the compositional range is presented. Regular, accessible mesoporous structures with local order are produced by simply mixing inorganic precursors in the presence of a high weight block copolymer. By resorting to milder condensation conditions (i.e., prehydrolysed silica precursors), highly ordered cubic mesostructures with sharp pore size distributions are obtained. The excellent interdispersion of both cations was probed by several spectroscopic techniques. In all samples, the Ti(IV) environment is close to that observed in amorphous systems, with a coordination number between 5 and 6. For high Si contents (80% or more), Ti ions present a mostly tetrahedral environment, substituting silicon centers, in agreement with previously reported data [65]. This high intermixing and porosity permits to tune the electronic density (thus, the refractive index), or even the chemical properties, such as the catalysis of silver reduction, permitting to control the extent of nanoparticle reduction within these matrices. As cleverly demonstrated by J. Livage and his school of thought, an accurate control of hydrolysis and condensation in sol-gel synthesis is the *"clef de voûte"* of the synthesis of complex materials with spatial ordering in several length scales.

Acknowledgements

This work has been funded by CONICET (PIP 5191, PIP 7631, PIP 3079) and ANPCyT (PICT 34518, 33581, PAE 2006 37063 00038), LNLS (SAXS, XRR, SXS and XAS projects) and Gabbos (GXNG 017). P.C.A. acknowledges a CNEA–CONICET joint graduate scholarship. M.C.F. and L.A. thank CONICET for graduate scholarships. N. De Vincenzo (CMA, FCEN, UBA) and P.B. Bozzano (UAM, CAC, CNEA) are gratefully acknowledged for the TEM images and EDS analysis. GJAASI and FGR are CONICET researchers.

Appendix A. Supplementary information

Supplementary data associated with this article can be found, in the online version, at doi:10.1016/j.crci.2009.07.001.

References

[1] *Chem. Mater.*, 2008, 20, Special Issue: Templated Materials, M. Jaroniec and F. Schüth Eds., pp. 599, and articles included.

[2] (a) G.J.A.A. Soler-Illia, C. Sanchez, B. Lebeau, J. Patarin, Chem. Rev. 102 (11) (2002) 4093 ;
(b) G.J.A.A. Soler-Illia, E.L. Crepaldi, D. Grosso, C. Sanchez, Curr. Opin. Colloid Interf. Sci. 8 (2003) 109.
[3] C. Sanchez, C. Boissière, D. Grosso, C. Laberty, L. Nicole, Chem. Mater. 20 (2008) 682.
[4] C.J. Brinker, Y. Lu, A. Sellinger, H. Fan, Adv. Mater. 11 (1999) 579.
[5] C.J. Brinker y, G.W. Scherer, Sol gel science. The physics and chemistry of sol gel processing, Academic Press, 1990.
[6] B.E. Yoldas, J. Non Cryst. Solids 38–39 (1980) 81.
[7] (a) See, for, example M.F. Best, R.A. Condrate, J. Mater. Sci. Lett. 4 (1985) 994 ;
(b) D.M. Pickup, G. Mountjoy, G.W. Wallidge, R. Anderson, J.M. Cole, R.J. Newport, M.E. Smith, J. Mater. Chem. 9 (1999) 1299.
[8] J.B. Miller, E.I. Ko, Catal. Today 35 (1997) 269.
[9] G.J.A.A. Soler Illia, E.L. Crepaldi, D. Grosso, C. Sánchez, J. Mater. Chem. 14 (2004) 1879.
[10] J.W. Kriesel, M.S. Sander, T.D. Tilley, Adv. Mater. 13 (2001) 331.
[11] S. Zhang, J. Wang, H. Liu, X. Wang, Catal. Commun. 9 (2008) 995.
[12] J.D. Bass, D. Grosso, C. Boissiere, E. Belamie, T. Coradin, C. Sanchez, Chem. Mater. 19 (2007) 4349.
[13] (a) P. Yang, D. Zhao, D.I. Margolese, B.F. Chmelka, G.D. Stucky, Nature 396 (1998) 152 ;
(b) P. Yang, D. Zhao, D.I. Margolese, B.F. Chmelka, G.D. Stucky, Chem. Mater. 11 (1999) 2813.
[14] S. Gontier, A. Tuel, Appl. Catal. A 143 (1996) 125.
[15] P.T. Tanev, M. Chibwe, T.J. Pinnavaia, Nature 368 (1994) 321.
[16] W. Zhang, M. Fröba, J. Wang, P.T. Tanev, J. Wong, T.J. Pinnavaia, J. Am. Chem. Soc. 118 (1996) 9164.
[17] M. Ogawa, K. Ikeue, M. Anpo, Chem. Mater. 13 (2001) 2900.
[18] J. El Haskouri, S. Cabrera, M. Gutierrez, A. Beltrán-Porter, D. Beltrán-Porter, M.D. Marcos, P. Amorós, Chem. Commun. (2001) 309.
[19] N. Hüsing, B. Launay, D. Doshi, G. Kickelbick, Chem. Mater. 14 (2002) 2429.
[20] E.L. Crepaldi, G.J.A.A. Soler-Illia, D. Grosso, F. Cagnol, F. Ribot, C. Sanchez, J. Am. Chem. Soc. 125 (2003) 9770.
[21] G.J.A.A. Soler Illia, E.L. Crepaldi, D. Grosso, D. Durand, C. Sánchez, Chem. Commun. (2002) 2298.
[22] www.lnls.br.(Instalações Abertas: Linhas de Luz: D11A-SAXS).
[23] A. van der Lee, Solid State Sci. 2 (2000) 257.
[24] (a) C. Boissière, D. Grosso, S. Lepoutre, L. Nicole, A. Brunet-Bruneau, C. Sanchez, Langmuir 21 (2005) 12362 ;
(b) A. Bourgeois, A.B. Bruneau, S. Fisson, B. Demarets, D. Grosso, F. Cagnol, C. Sanchez, Rivory, J. Thin Solid Films 447 (2004) 46 ;
(c) M.R. Baklanov, K.P. Mogilnikov, V.G. Polovinkin, F.N. Dultsev, J. Vac. Sci. Technol. B 18 (2000) 1385.
[25] T.W. Kim, R. Ryoo, M. Kruk, K.P. Gierszal, M. Jaroniec, S. Kamiya, O. Terasaki, J. Phys. Chem. 108 (2004) 11480.
[26] www.lnls.br (Instalações Abertas: Linhas de Luz: D04B-XAS).
[27] B.K. Teo, EXAFS: basic principles and data analysis, Springer, New York, 1986.
[28] R. Brydson, H. Sauer, W. Engel, J.M. Thomas, E. Zeitler, N. Kosugi, H. Kuroda, J. Phys. Condens. Mater. 1 (1989) 797.
[29] J.C. Parlebas, M.A. Khan, T. Uozumi, K. Okada, A. Kotani, J. Electron Spect. Related Phen. 71 (1995) 117.
[30] V. Luca, S. Djanjanti, R.F. Howe, J. Phys. Chem. B 5 (1998) 118.
[31] J. Stöhr, NEXAFS Spectroscopy, Springer, New York, 1992.
[32] P.C. Angelomé, L. Andrini, M.E. Calvo, F.G. Requejo, S.A. Bilmes, G.J.A.A. Soler-Illia, J. Phys. Chem. C 111 (2007) 10886.
[33] www.lnls.br (Instalações Abertas: Linhas de Luz: D04A-SXS).
[34] M.C. Fuertes, M. Marchena, M.C. Marchi, A. Wolosiuk, G.J.A. A: Soler-Illia, Small 5 (2009) 272.
[35] P.C. Angelomé, Mesoporous metallic, mixed and hybrid oxide thin films. Towards a rational design of functional nanomaterials, Ph. D. Thesis, University of Buenos Aires, Argentina, **2008**, Chapter 3.
[36] V. Luca, G.J.A.A. Soler-Illia, P.C. Angelomé, P.Y. Steinberg, E. Drabarek, T.L. Hanley, Microporous Mesoporous Mater. 118 (2009) 443.
[37] G.J.A.A. Soler-Illia, P. Innocenzi, Chem. Euro. J. 12 (2006) 4478.
[38] S. Diré, F. Babonneau, C. Sánchez, J. Livage, J. Mater. Chem. 2 (1992) 239.
[39] D. Hoebbel, T. Reinert, H. Schmidt, J. Sol-Gel Sci. Technol. 7 (1996) 217.
[40] J.S. Rigden, J.K. Walters, P.J. Dierken, M.E. Smith, G. Bushnell-Wye, W.S. Howells, R.J. Newport, J. Phys. Condens. Mater. 9 (1997) 4001.
[41] P. Innocenzi, J. Non Cryst. Sol. 316 (2003) 309.
[42] M. Andrianainarivelo, R. Corriu, D. Leclercq, P. H: Mutin, A. Vioux, J. Mater. Chem. 6 (1996) 1665.
[43] Z. Zhan, H.C. Zeng, J. Non Cryst. Solids 243 (1999) 26.
[44] J.M. Miller, L.J. Lakshmi, J. Phys. Chem. B 102 (1998) 6465.
[45] S.H. Teo, H.C. Zeng, J. Phys. Chem. B 105 (2001) 9093.
[46] (a) V.A. Zeitler, C.A. Brown, J. Phys. Chem. 61 (1957) 1174 [Proposed for the first time for Ti containing siloxanes and silanes in] ;
(b) In mixed oxides, see for example C.F. Smith, S.A. Condrate, W.E. Votava, Appl. Spectroscopy, 29 (1975) 79 ;
(c) D.C.M. Dutoit, M. Schneider, A. Baiker, J. Catal. 153 (1995) 165.
[47] P. Wu, T. Komatsu, T. Yashima, J. Phys. Chem. 100 (1996) 10316.
[48] S. Klein, S. Thorimbert, W.F. Maire, J. Catal. 163 (1996) 476.
[49] C. Beck, T. Mallat, T. Bürgi, A. Baiker, J. Catal. 204 (2001) 428.
[50] R.J. Davis, Z. Liu, Chem. Mater. 9 (1997) 2311.
[51] X. Gao, I.E. Wachs, Catal. Today 51 (1999) 233.
[52] F. Farges, G.E. Brown Jr., J.J. Rehr, Phys. Rev. B 56 (1997) 1809.
[53] T. Uozumi, K. Okada, A. Kotani, O. Durmeyer, J.P. Kappler, E. Beaurepaire, J.C. Parlebas, Europhys. Lett. 18 (1992) 85.
[54] N. Jiang, D. Su, C.H. Spence, Phys. Rev. B 76 (2007) 214117.
[55] L.A. Grunes, Phys. Rev. B 27 (1983) 2111.
[56] C. Belver, R. Bellod, S.J. Stewart, F.G. Requejo, M. Fernández-García, Applied Cat. B 65 (2006) 309.
[57] (a) J.M. Notestein, L.R. Andrini, V.I. Kalchenko, F.G. Requejo, A. Katz, E. Iglesia, J. Am. Chem. Soc. 129 (2007) 1122 ;
(b) J.M. Notestein, A. Solovyov, L.R. Andrini, F.G. Requejo, A. Katz, E. Iglesia, J. Am. Chem. Soc. 129 (2007) 15585.
[58] G. Mountjoy, D.M. Pickup, G.W. Wallidge, R. Anderson, J.M. Cole, R.J. Newport, M.E. Smith, Chem. Mater. 11 (1999) 1253.
[59] A. Bianconi, M. Dell'Ariccia, A. Gargano, C.R. Natoli, *Bond Length using XANES*, en Proceedings of the 1st International Conference on EXAFS and XANES, Springer, New York1983.
[60] M.N. Piancastelli, J. Electron Spect. Related Phen. 100 (1999) 167.

[61] G. Mountjoy, D.M. Pickup, R. Anderson, G.W. Wallidge, M.A. Holland, R.J. Newport, M.E. Smith, Phys. Chem. Chem. Phys. 2 (2000) 2455.
[62] C. Levelut, D. Cabaret, M. Benoit, P. Jund, A.-M. Flank, J. Non Crystall. Solid. 293 (2001) 100.
[63] D. Lie, G.M. Bancroft, M. Kasrai, M.E. Fleet, R.A. Secco, X.H. Feng, K.H. Tan, B.X. Yang, Am. Mineral 79 (1994) 622.
[64] M.D. Pérez, E. Otal, S.A. Bilmes, G.J.A.A. Soler-Illia, E.L. Crepaldi, D. Grosso, C. Sanchez, Langmuir 20 (2004) 6879.
[65] M. Takeuchi, M. Matsuoka, H. Yamashita, M. Anpo, J. Synchrotron Rad. 8 (2001) 643.
[66] V. Lafond, P.H. Mutin, A. Vioux, Chem. Mater. 16 (2004) 5380.
[67] A. Corma, M.T. Navarro, J. Pérez Pariente, J. Chem. Soc. Chem. Commun. (1994) 147.